THE O- AND B-TYPE STELLAR POPULATION IN W3: BEYOND THE HIGH-DENSITY LAYER

Megan M. Kiminki[1], Jinyoung Serena Kim[1], Micaela B. Bagley[1,2], William H. Sherry[3,4], and George H. Rieke[1]
Accepted to ApJ: *30 August 2015*

ABSTRACT

We present the first results from our survey of the star-forming complex W3, combining VRI photometry with multiobject spectroscopy to identify and characterize the high-mass stellar population across the region. With 79 new spectral classifications, we bring the total number of spectroscopically-confirmed O- and B-type stars in W3 to 105. We find that the high-mass slope of the mass function in W3 is consistent with a Salpeter IMF, and that the extinction toward the region is best characterized by an R_V of approximately 3.6. B-type stars are found to be more widely dispersed across the W3 giant molecular cloud (GMC) than previously realized: they are not confined to the high-density layer (HDL) created by the expansion of the neighboring W4 H II region into the GMC. This broader B-type population suggests that star formation in W3 began spontaneously up to 8–10 Myr ago, although at a lower level than the more recent star formation episodes in the HDL. In addition, we describe a method of optimizing sky subtraction for fiber spectra in regions of strong and spatially-variable nebular emission.

Subject headings: dust, extinction — open clusters and associations: individual (Westerhout 3) — stars: early-type — stars: formation — stars: luminosity function, mass function

1. INTRODUCTION

Massive stars have a dramatic impact on their environment, affecting the surrounding matter distribution and energy budget through their winds, ionizing radiation, and eventually supernovae. They influence processes on scales ranging from the reionization of the universe to the timescale of circumstellar disk dispersal. One notable effect of massive star feedback may be the triggering of new generations of star formation, either by sweeping neighboring molecular gas into a dense shell which subsequently fragments into pre-stellar cores (e.g., Elmegreen & Lada 1977; Whitworth et al. 1994; Elmegreen 1998) or by compressing existing dense clumps past the point of gravitational instability (e.g., Sandford et al. 1982; Bertoldi 1989).

The W3 star-forming region (Westerhout 1958) is a group of H II regions and luminous infrared sources located in the outer Galaxy. Its distance of 2.0 kpc has been well established by maser parallax measurements (Hachisuka et al. 2006; Xu et al. 2006). W3 is associated with a giant molecular cloud (GMC) of mass 4×10^5 $M_\odot$ (Polychroni et al. 2012). The GMC borders on the extensive H II region W4, which is currently being ionized by the young cluster IC 1805 (Massey et al. 1995). Considered a classic case of probable triggered star formation (Lada et al. 1978; Carpenter et al. 2000; Oey et al. 2005; Ruch et al. 2007; Feigelson & Townsley 2008), the W3/W4 complex has long been the focus of massive-star and star-formation research (see Megeath et al. 2008, and references therein).

The edge of the W3 GMC has been compressed by the expanding W4 H II region into a high-density layer (HDL; Lada et al. 1978), which contains about half of the total mass of the cloud (Polychroni et al. 2012). Along this interface lies a sequence of star-forming sub-regions, of which the most visibly prominent is IC 1795 (see Figure 1). At 3–5 Myr old, IC 1795 is the oldest of the clusters in W3's HDL (Oey et al. 2005; Roccatagliata et al. 2011). Its H II region appears to have contributed to triggering the formation of its younger neighbors, W3(OH) and W3 Main (Oey et al. 2005), although it has been argued (Feigelson & Townsley 2008) that W3 Main's spherical shape favors a spontaneous star-formation scenario instead. South of the other sub-regions lies AFGL 333, another site of active star formation that appears to have been triggered by the expansion of W4 into the W3 GMC (Rivera-Ingraham et al. 2011).

Much of the study of W3 to date has focused on the clusters in the HDL, but recent results have begun to probe a more widespread and relatively older stellar population. Rivera-Ingraham et al. (2011) detected groups of relatively older young stars to the west of W3 Main and AFGL 333, suggesting a prior generation of star formation not triggered by feedback from W4. Similarly, Román-Zúñiga et al. (2011) saw evidence in the K-band luminosity function for an 8-Myr-old population near W3(OH). The simple picture of the W3/W4 complex as a sequence of triggered clusters may not be as clean as it initially appears.

In this paper, we present the first results of our survey of the full stellar content of W3, focusing here on the high-mass population. We describe our photometric and spectroscopic observations (including our approach to removing sky emission from stellar spectra) in Section 2 and discuss the identification, classification, and spatial distribution of O- and B-type stars in Section 3. In Section 4, we put constraints on the extinction law toward W3, which we use in Section 5 to estimate stellar parameters and construct an H-R diagram. The high-mass

[1] Steward Observatory, University of Arizona, 933 North Cherry Avenue, Tucson, AZ 85721, USA; mbagley@email.arizona.edu
[2] Minnesota Institute for Astrophysics, School of Physics and Astronomy, University of Minnesota, 116 Church Street S.E., Minneapolis, MN 55455, USA
[3] National Optical Astronomy Observatories, 950 North Cherry Avenue, Tucson, AZ 87719, USA
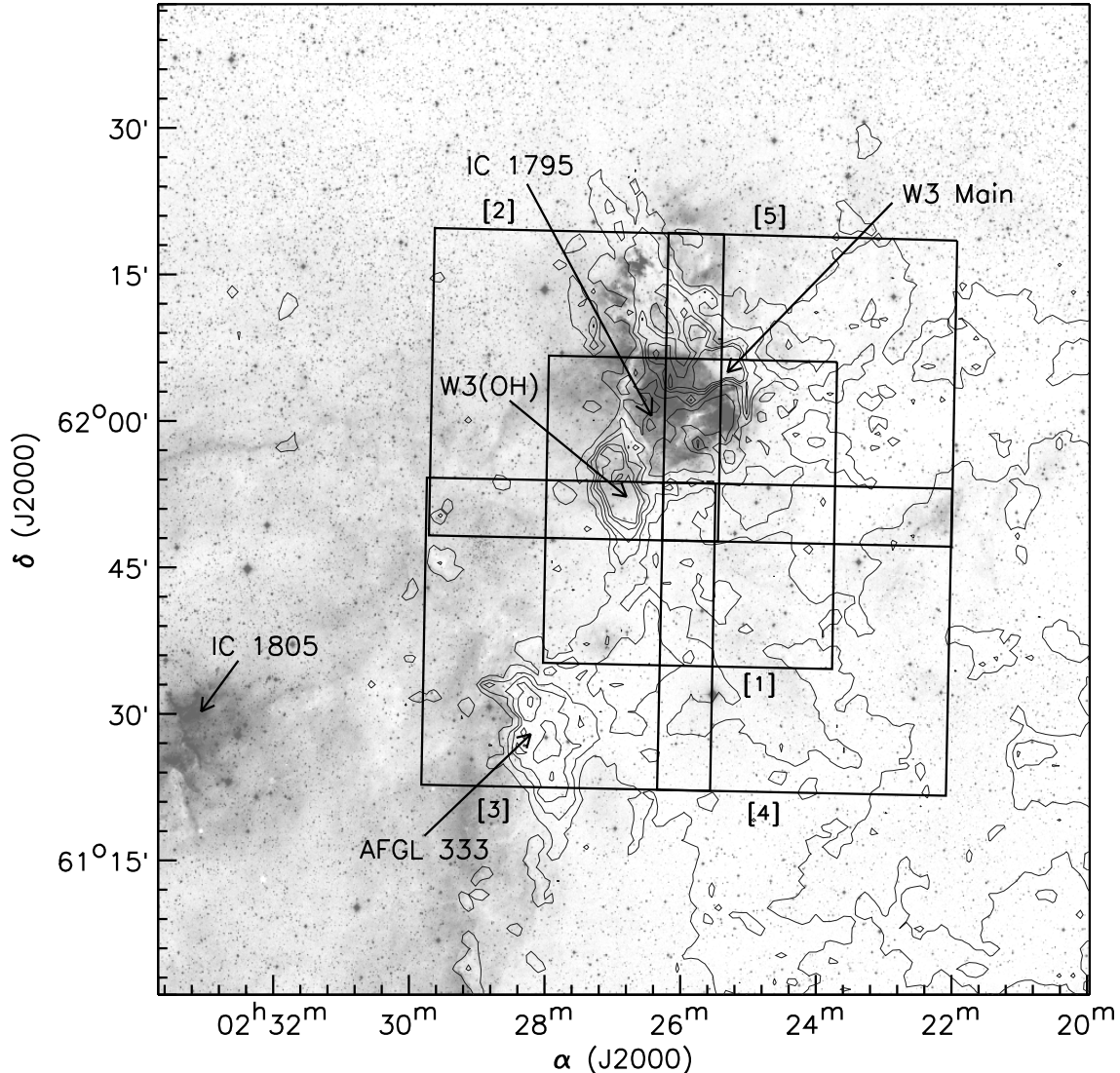[4] Eureka Scientific, 2452 Delmer Street Suite 100, Oakland, CA 94602, USA

Figure 1. Image of the W3/W4 complex from the Digitized Sky Survey (DSS) with ^{12}CO $J = 2$–1 contours from Bieging & Peters (2011), along with outlines of the five dither positions used in our 2005 90Prime imaging. IC 1805 (W4) and the major features of the W3 HDL are labeled.

initial mass function (IMF) for W3 is presented in Section 6. Finally, we discuss the implications of our results in the context of W3's star-formation history in Section 7.

2. OBSERVATIONS AND DATA REDUCTION

2.1. *Optical Photometry*

We observed W3 with the 90Prime wide-field imager (Williams et al. 2004) at the Steward Observatory 2.3-m Bok Telescope on 2005 October 7. 90Prime consists of four 4k × 4k CCDs, each with a field of view of $\sim 30' \times 30'$ and a pixel scale of $0.45''$ pix^{-1}. Due to weather constraints and CCD failure, we were only able to use data from the single chip (Chip 2) for which we obtained adequate standard star coverage. Combining five dithered observations, shown in Figure 1, gave us roughly one square degree of coverage in Cousins/Bessell V and I, with dithers 1–4 also observed in R. Each dither consisted of a 30-s exposure in V, a 5-s exposure in R, and

a 5-s exposure in I, except for dither 1 for which the I-band exposure was 7 s long. The seeing of the observations ranged from $1.2''$ to $1.9''$ with a median of $1.5''$.

A more complete discussion of our imaging observations and photometry will be the subject of an upcoming paper (J. Jose et al., in preparation). Briefly, we performed standard data reduction procedures, measured photometry, and applied aperture corrections using the IDL pipelines *Bokproc*, *Bokphot*, and *aperture_correct*, which are designed for use on 90Prime images (W. H. Sherry et al., in preparation). Aperture corrections were fit across each image using IDL's built-in routine for minimum curvature surface interpolation. Because the aperture corrections varied strongly across 90Prime's large field of view, we processed and measured photometry on each dithered image separately and merged the photometric catalogs post-calibration. The most prominant saturated stars were automatically removed during the reduction pipeline, and additional saturated stars and
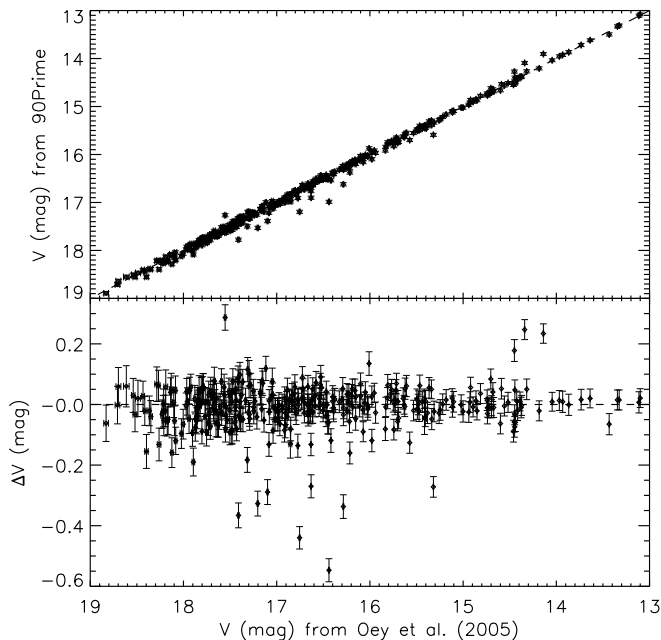
Figure 2. Comparison of our 90Prime V magnitudes with those of Oey et al. (2005) for the 354 stars for which overlapping photometry is available.

stars that overlapped diffraction spikes or bad columns were identified manually and flagged in the resulting catalog. We calibrated our instrumental magnitudes using same-night observations of the SA 92 and SA 98 standard fields (Stetson 2000).[5] The standard fields were observed under comparable seeing conditions at a range of airmasses bracketing the target airmass. We then fit the slope of the color term for the photometric calibration as a function of airmass.

We measured V and I photometry for $\sim 22,000$ sources, complete down to $V \sim 20$ mag. In Figure 2, we compare our V photometry with that of Oey et al. (2005), who imaged stars in and around IC 1795. Of the 399 stars in the Oey et al. (2005) catalog, we have unsaturated V photometry of 354, all with $13 > V > 19$. Our magnitudes differ from theirs by a mean of -0.01 mag, with an rms scatter of 0.08 mag. We thus consider our photometry to be in good agreement with that of Oey et al. (2005).

2.2. *Spectroscopy*

We targeted candidate members of W3 for spectroscopic follow-up with the Hectospec multi-fiber spectrograph (Fabricant et al. 2005) on the 6.5-m MMT. Spectroscopic targets were selected on the basis of their location in the V, $V - I$ color-magnitude diagram (Figure 3) relative to the Siess et al. (2000) solar-metallicity pre-main-sequence (PMS) isochrones. For the purposes of target selection, the PMS isochrones were corrected for a distance of 2.0 kpc and a foreground extinction of $A_V = 2.6$ mag. Sources lying redward of the 5 Myr PMS isochrone were prioritized when creating Hectospec fiber pointings, with sources redward of the 2 Myr PMS

isochrone given the highest priority. These target selection criteria were designed to minimize the number of foreground stars observed spectroscopically: a model foreground population from the Besançon Galactic model (Robin et al. 2003, assuming an average extinction of $A_V = 1.3$ mag kpc^{-1}), predicts that more than 90% (80%) of the expected foreground population toward W3 lies blueward of the 2 Myr (5 Myr) Siess et al. (2000) isochrones. These target selection criteria also prioritized the color-magnitude space occupied by O-type and early/mid B-type stars (see Figure 3 and discussion in Section 3.2).

Thirty-one Hectospec fiber configurations were observed in queue mode over 27 nights from 2008 to 2012. Exposure times were chosen to achieve a minimum signal-to-noise (S/N) ratio of 25 at 6500 Å. The acheived S/N ranged between 22 and 132, with a median of 45. Details of each fiber configuration (date of observation, center of field of view, grating, total on-source exposure time, and number of targets observed) are given in Table 1. A total of 1577 sources were observed one or more times with Hectospec's 270 lines mm^{-1} (lpm) grating, which provides ~ 5 Å resolution at 3650–9200 Å. As shown in Figure 3, these sources included the majority of objects lying redward of the 5 Myr Siess et al. (2000) PMS isochrone with $13 < V \leq 18.5$ mag, as well as several hundred sources with $V > 18.5$ mag (not shown). A randomly-chosen subset of 886 targets were also observed with the the 600 lpm grating centered on Hα, which provides ~ 2 Å resolution at 5000–7800 Å.

Spectroscopic data were reduced using Juan Cabanela's E-SPECROAD[6], an external version of the Hectospec SPECROAD pipeline (Mink et al. 2007). The E-SPECROAD pipeline automates a set of Hectospec-specific IRAF[7] tasks that perform basic data reduction: bias and dark-current subtraction, flat-fielding, merging of four amplifier outputs into one image, aperture extraction, cosmic ray removal, and combination of multiple exposures. The pipeline also corrects for atmospheric water absorption and red light leaks from the Hectospec fiber-positioning robots. Wavelength calibration was performed in IRAF using HeNeAr or HgNeAr calibration lamp exposures from each night's observations. As discussed below, we did not use the E-SPECROAD sky subtraction procedure because the complexity of the W3 field required a more sophisticated sky subtraction algorithm.

2.3. *Sky Subtraction*

Unlike long-slit spectrographs, fiber spectrographs like Hectospec do not produce simultaneous observations of the sky emission immediately adjacent to the science target. Typically, some fraction of the fibers in each pointing are placed on blank sky and their spectra are combined into a master spectrum of sky emission lines, to be subtracted from every science spectrum. This method was not suitable for W3 because of the strong, spatially-
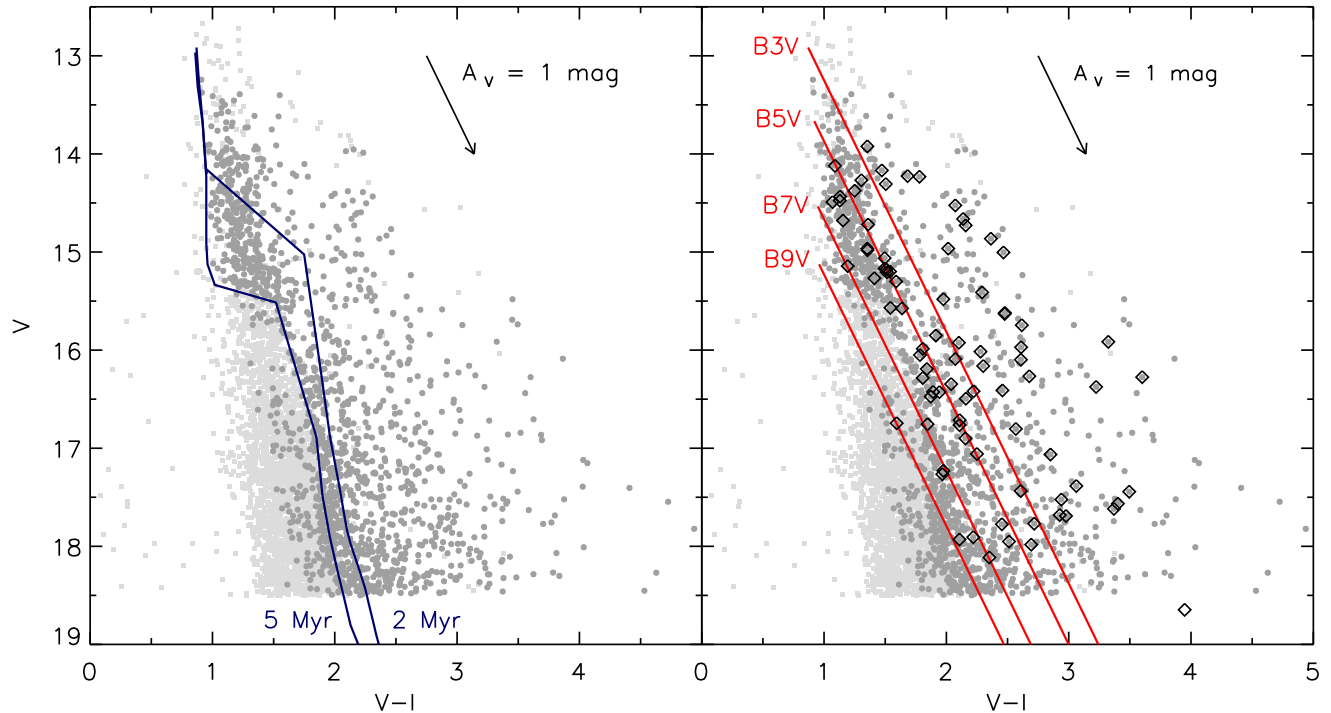
Figure 3. Left: $V, V - I$ color-magnitude diagram of 90Prime sources in W3 with $V \leq 18.5$ mag. Sources with Hectospec spectra are denoted by dark grey filled circles, while 90Prime sources that were not targeted for spectrosopic follow-up are shown as light grey filled squares. The solid blue lines are the reddened 2 and 5 Myr pre-main-sequence isochrones from Siess et al. (2000) that were used in target selection. Right: The same color-magnitude diagram with identified O- and B-type stars (see Section 3) highlighted with open diamonds. Overplotted are the reddening tracks (red lines) for B3, B5, B7, and B9 V stars using the extinction law from Section 4.

variable nebular emission from its multiple H II regions. Each Hectospec fiber subtends $1.5''$, capturing the contribution from a small patch of sky around the target star, including the nebular emission lines. As illustrated in Figure 4, incomplete subtraction of these nebular lines is particularly problematic for the assessment of the nature of Hα absorption/emission in a source.

For each Hectospec pointing, we took an additional exposure shifted $5''$ from the science targets, giving each star a corresponding sky offset spectrum. To maximize our observing efficiency, the duration of these sky offset exposures was 1/3 to 1/5 of the total exposure time spent on-source. Consequently, as shown in Figure 5, directly subtracting the sky offset spectra produced a noticeable decrease in the S/N of the output. We therefore developed our own IDL-based sky subtraction pipeline to maximize the S/N and accuracy of the resultant spectra.[8]

Our sky subtraction pipeline first screens for and excludes any sky fibers whose spectra are contaminated by nearby stars. All remaining sky spectra from a given Hectospec pointing are median-combined into a master sky. The nebular emission lines (Hα; Hβ; [O III] $\lambda\lambda4959, 5007$; [N II] $\lambda\lambda6547, 6583$; [S II] $\lambda\lambda6716, 6731$; and, when present above the noise level, He I $\lambda\lambda5876, 6678, 7065$ and [Ar III] $\lambda7135$) are fit with Gaussian profiles using the MPFIT package (Markwardt 2008) and subtracted from the master sky to produce a *"master-minus-nebular"* template. The *master-minus-nebular* spectrum is sub-

tracted from each individual sky spectrum, leaving a residual containing only the local nebular emission lines. These nebular lines are also fit with Gaussian profiles, and those profiles are added to the *master-minus-nebular* template to produce a high-S/N *"synthetic sky"* spectrum. It is this *synthetic sky* that is subtracted from the corresponding stellar spectrum.

This sky subtraction method accurately subtracts the nebular emission lines (see Figure 4) while increasing the continuum S/N of the output spectra by an average of 30% relative to directly subtracting the sky offset spectra (see Figure 5). However, as with the simpler options, this method does not accurately subtract auroral lines such as [O I] $\lambda\lambda5577, 6300$. These lines vary too rapidly in time and space to be accurately removed from spectra taken with a fiber spectrograph.

An additional product of our sky subtraction pipeline is information on the level of Hα emission across the observed field. Figure 6 is a contour map of the nebular Hα emission measured in 6083 sky spectra. The H II region created by IC 1795 is clearly visible near the center of the map, and the northwest part of the W4 H II region is evident to the west.

3. THE O- AND B-TYPE STARS IN W3

3.1. *Spectral Classification*

We identified and classified O- and B-type stars via a two-step process. First, we screened the spectra of all 1577 Hectospec targets for the presence of He I in absorption or emission at 4471, 5876, 6678, and/or 7065 Å. All stars with plausible He I lines were flagged for

---

[8] The latest version of our sky subtraction pipeline is available at https://github.com/mkiminki/hectosky.

Table 1
Hectospec Observing Details

Date (UT)	α (J2000)[a] (HH:MM:SS.s)	δ (J2000)[a] ($° : ' : ''$)	Grating (lines mm^{-1})	Exposure Time (minutes)	# Science Fibers
2008 Dec 4	02:26:38.0	+61:53:36	600	30	176
2008 Dec 4	02:26:50.2	+61:48:11	600	60	183
2008 Dec 5	02:26:59.1	+61:47:15	600	60	154
2008 Dec 7	02:26:19.8	+61:51:29	600	120	217
2009 Feb 3	02:27:06.2	+61:49:57	600	30	179
2009 Feb 3	02:27:14.6	+61:49:57	600	120	213
2009 Feb 5	02:26:15.7	+61:58:46	600	60	101
2009 Feb 5	02:27:16.2	+61:49:13	600	60	99
2009 Mar 2	02:27:19.5	+61:49:42	600	120	213
2009 Oct 11	02:26:11.0	+61:59:19	270	60	205
2009 Oct 16	02:26:40.4	+61:57:01	600	120	215
2009 Oct 17	02:26:35.4	+61:56:55	270	18	207
2009 Dec 12	02:27:12.8	+61:51:10	270	18	178
2009 Dec 15	02:27:07.5	+61:49:41	600	120	163
2010 Oct 2	02:26:43.5	+61:53:22	270	45	160
2010 Oct 3	02:28:11.0	+61:40:37	270	45	152
2010 Oct 10	02:27:16.9	+61:42:32	270	45	183
2010 Oct 10	02:26:58.5	+62:05:53	270	45	128
2010 Oct 11	02:25:43.1	+62:03:14	270	40	139
2010 Oct 16	02:25:40.7	+62:00:25	270	51	128
2010 Oct 17	02:25:36.1	+61:43:10	270	36	134
2010 Nov 26	02:27:17.1	+61:42:08	600	80	186
2010 Nov 27	02:25:11.3	+61:44:38	600	80	224
2011 Sept 20	02:25:38.6	+61:52:04	270	21	154
2011 Oct 24	02:25:19.4	+61:58:54	270	51	172
2011 Oct 25	02:26:55.5	+62:00:35	270	66	107
2011 Nov 17	02:26:13.6	+61:54:21	270	30	84
2011 Nov 18	02:25:29.3	+61:36:18	270	60	54
2012 Jan 23	02:27:12.9	+61:56:09	270	150	222
2012 Feb 11	02:25:50.9	+61:47:28	270	150	231
2012 Feb 12	02:26:24.5	+61:49:21	270	150	222

[a] Positions are given for the center of the Hectospec field of view for the given fiber configuration.

further analysis. In cases where the presence of He I was debatable, we considered the progression of the higher-order Paschen lines at 8500–9100 Å: if the Paschen lines did not show any blending with the Ca II triplet, we flagged the star for further analysis.

This screening procedure resulted in a list of 91 candidate O- and B-type stars in W3. It is likely that some of the latest-type B stars (B8–B9) present in our Hectospec sample were missed, as these stars exhibit relatively weak He I absorption. Very early-type O stars (O3–O4) also have weak He I lines and could theoretically been missed as well; however, given their intrinsic brightness, it is unlikely that there are any unknown O3–O4 stars at the distance of W3. As discussed in Section 3.2, the brightest mid-type O stars in W3 were saturated in our 90Prime photometry, were not targeted for followup spectroscopy, and are added to our final sample from the literature.

Next, the spectral types of the candidate O- and B-type stars were determined by visual comparison of their continuum-normalized spectra to the spectra of standard stars from Gray & Corbally (2009), which are at comparable resolution (3.6 Å). Figure 7 displays the 270 lpm spectra of five sources illustrative of the range of spectral types analyzed. The key features considered in classification were: for O-type stars, the ratios of He II to He I line strengths; for all B-type stars, the size and shape of the He I lines relative to the hydrogen Balmer lines; and for B4-B9 stars, the ratio of He I $\lambda 4471$ to Mg II $\lambda 4481$. The spectral type of most stars in our sample could be

determined to within 1–2 temperature subclasses. Our Hectospec spectra did not resolve the metal lines often used for more precise classification, such as Si IV, Si III, and Si II lines in B0-B3 stars (Walborn & Fitzpatrick 1990).

The spectral resolution was also insufficient to reliably distinguish between dwarf and giant luminosity classes (we could have identified supergiants, but found none). Stars are therefore assumed to be dwarfs except for one case where multiple authors agreed that the narrow width of the Balmer lines could only be fit by a giant type. The effect of this assumption on our derived stellar parameters (see Section 5) is negligible.

Table 2 lists the coordinates, spectral types, and 90Prime photometry of the 91 candidate O- and B-type stars. Four of the candidate O- and B-type stars were found to be early A-type stars and are listed as such. In addition, we were unable to further classify ten of the candidate O- and B-type stars because their spectra were too noisy or too heavily-extincted in the critical 4000–5000 Å range. However, all ten stars exhibited clear He I absorption or emission at 6678 and 7065 Å (see Figure 8 for an example). For three of these stars, spectral types derived from K_s-band spectra are available in the literature (see Section 3.2); the remaining seven are listed in Table 2 as "B:" stars.

3.2. Additional Stars from the Literature

Oey et al. (2005), Navarete et al. (2011), and Bik et al. (2012) spectroscopically identified a com-
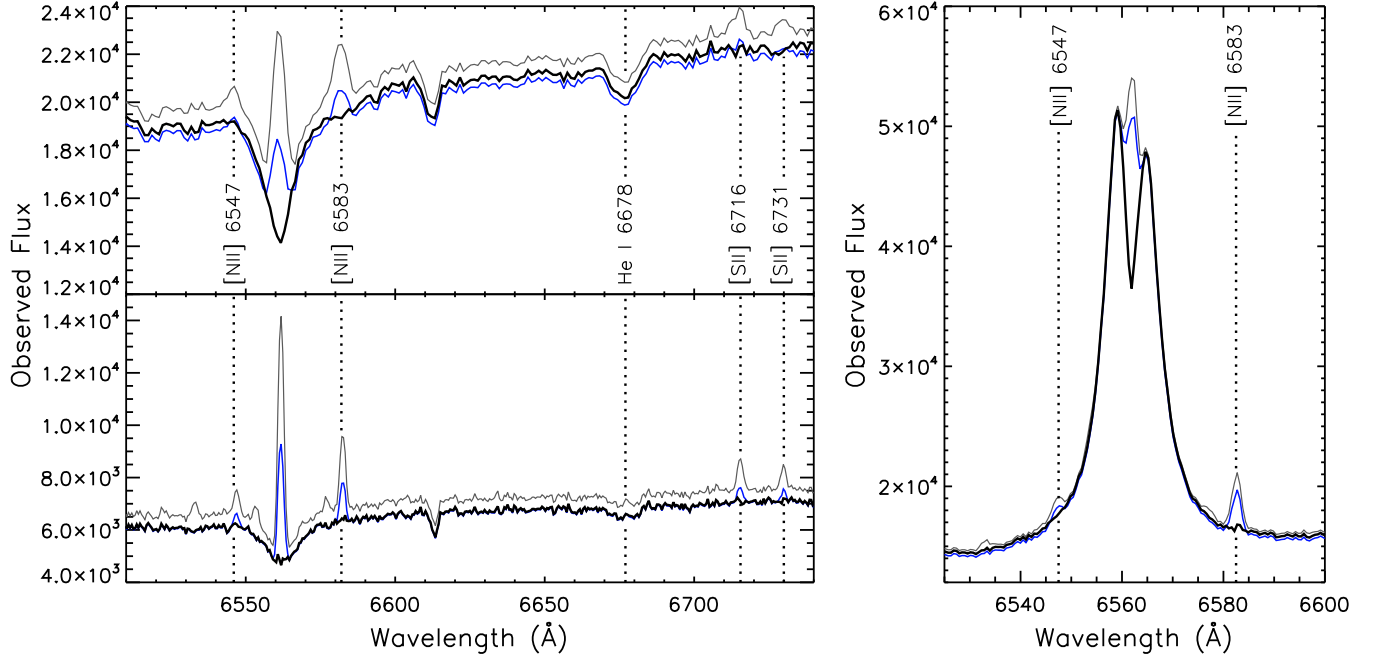
Figure 4. Left: Spectra of an example B-type star (source 15 in Table 2), comparing the result of no sky subtraction (grey), subtraction of a master sky spectrum (blue), and sky subtraction via the method described in Section 2.3 (thick black spectrum). The top spectrum was taken with Hectospec's 270 lines mm^{-1} (lpm) grating; the bottom spectrum is the same object observed with the 600 lpm grating. Nebular emission lines (except for Hα) and relevant spectral features are labeled. Right: Same as left for a source with intrinsic Hα emission (source 65 in Table 2).
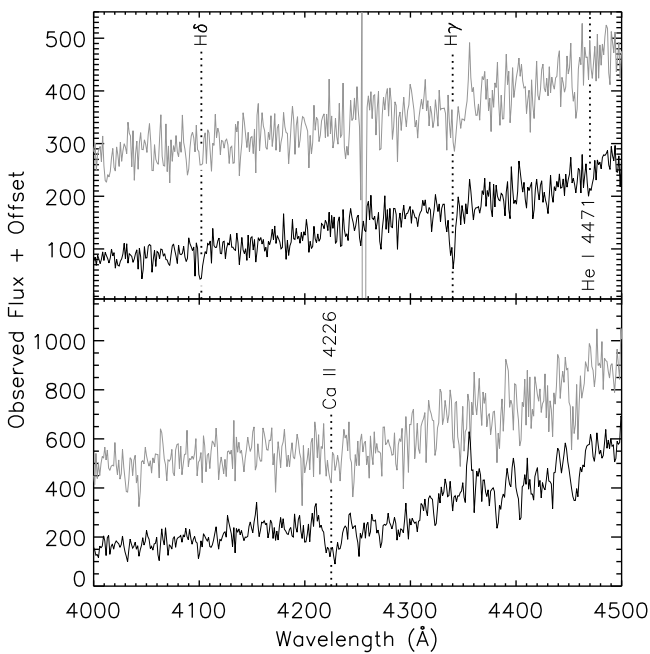

Figure 5. Examples of the improvement in signal-to-noise achieved by our sky subtraction method (black) compared to directly subtracting the sky offset spectra (grey). The spectra are offset for clarity. Some key lines used in the classification of a B-type star (top; source 52 in Table 2) and a K-type star (bottom) are marked.

Figure 6. Map of Hα emission across W3 measured from 6083 Hectospec sky spectra (270 lpm). The bright central region is IC 1795; the left edge of the image is part of the W4 H II region. The equivalent widths have an average uncertainty of ± 1 Å.

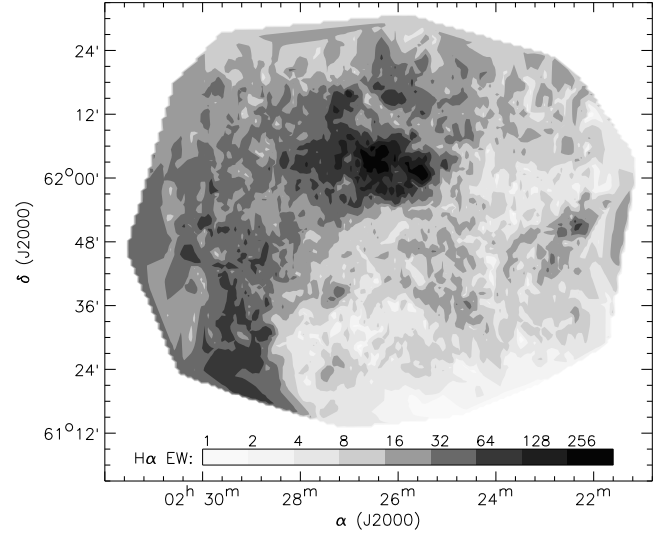bined total of 24 O- and B-type stars in W3. Our Hectospec observations included nine of those sources, eight of which show He I lines at optical wavelengths and were included in our initial list of high-mass stars. We were able to determine spectral types for five of those eight, and our types are in good agreement with the literature (within $\pm$ one temperature subtype). We adopt the literature classifications for the three in our sample for which we were unable to determine precise spectral types, and for the 15 stars not included in our sample. For spatial completeness, we also add the two massive stars from Massey et al. (1995)'s survey of IC
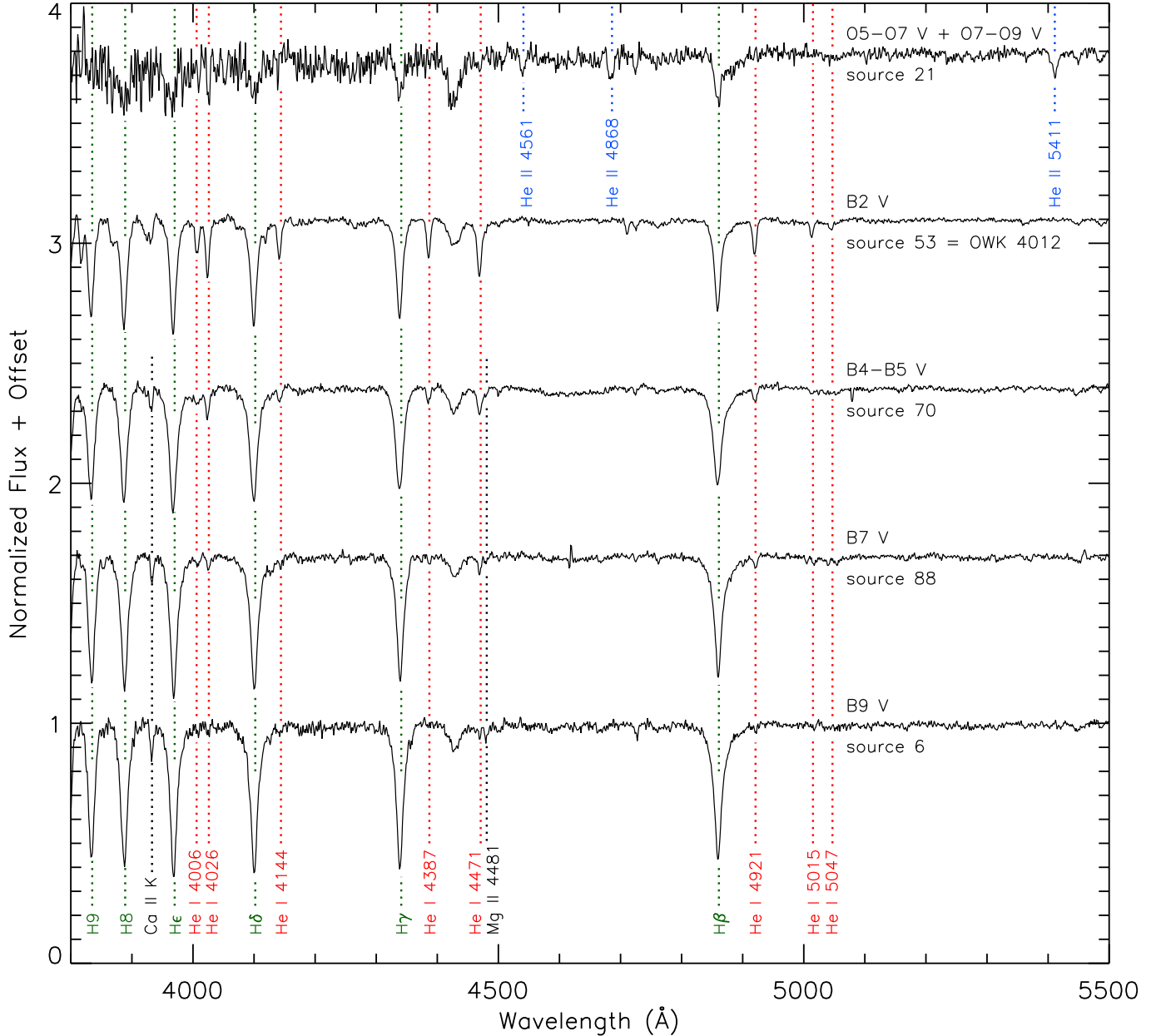
Figure 7. Normalized spectra of representative O- and B-type systems in W3. Dotted lines mark the key features used in spectral classification (green: hydrogen; red: He I; blue: He II; black: metals). All spectra in this figure were taken using Hectospec's 270 lines mm^{-1} grating.

1805 (W4) that fall within our 90Prime field of view but were not targeted with Hectospec.

The magnitude distribution of the high-mass stars added from the literature demonstrates the completeness limits of our Hectospec sample. On the bright end, our observations excluded stars with $V < 13$ mag, because these sources were saturated in our 90Prime images. On the faint side, our completeness varies with spectral type and extinction (see Figure 3). Including the O- and B-type stars detected by Navarete et al. (2011) and Bik et al. (2012) in K_s, which those groups classified based on their near-infrared spectra, extends our sample but further complicates an assessment of our completeness, particularly as those surveys focused on W3 Main and the HDL and did not explore the rest of the

W3 GMC. We also choose to exclude the youngest and most embedded objects in W3, as we focus on stars that have reached or are close to reaching the zero-age main sequence. For example, we leave out the three deeply-embedded, massive young stellar objects (YSOs) identified by Bik et al. (2012) in W3 Main, along with the several massive protostars known to be embedded in the infrared-bright source W3(OH) (e.g., Hirsch et al. 2012).

In total, there are 105 spectroscopically-confirmed O- and B-type stars in W3. Of these, 98 have well-constrained spectral types from this work or the literature, and 92 of those have optical photometry sufficient to compute their luminosities and place them on a Hertzsprung-Russell diagram for comparison to stellar evolution models.
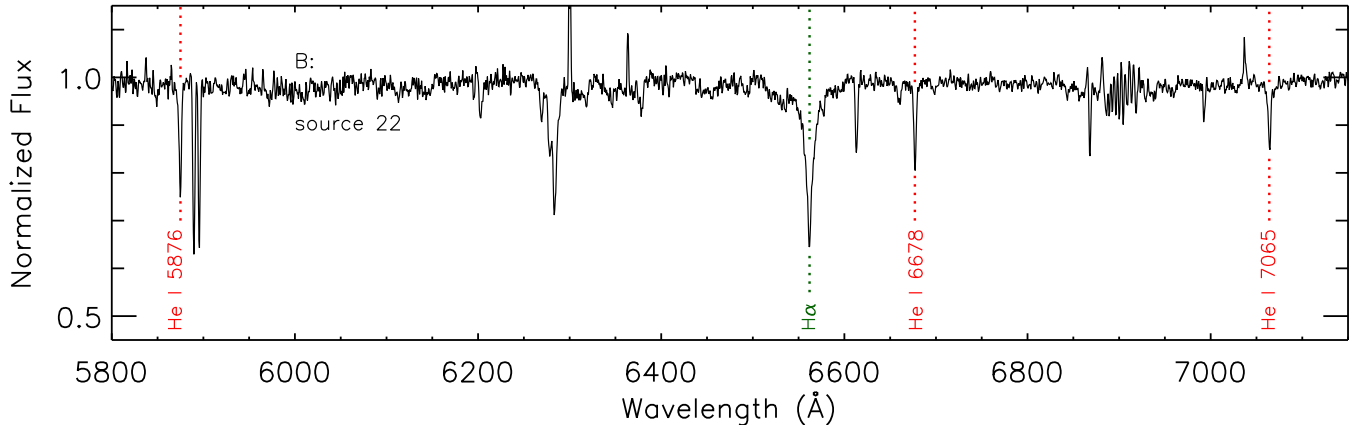
Figure 8. Normalized spectrum of a representative B: star, as observed with Hectospec's 600 lines mm^{-1} (lpm) grating. Relevant spectral features are marked as in Figure 7. The B: sources cannot be classified using the wavelength range shown in Figure 7 because their 270 lpm spectra are overly noisy or they are heavily extincted in the blue. Consequently, we were unable to determine precise spectral types for these sources, although their He I absorption lines identify them as B-type (or possibly late O-type) stars. Most of the unmarked features in this spectrum are of interstellar or atmospheric origin.

3.3. *Infrared Counterparts*

Using a $1''$ source-matching radius, we identify the Two Micron All Sky Survey (2MASS; Skrutskie et al. 2006) JHK_s counterparts to our sources. All sources from our data and the literature have 2MASS counterparts except for IRS N6. We exclude 2MASS magnitudes with a signal-to-noise < 5 (i.e., sources with flags D, E, F, or X) from further analysis. For stars in W3 Main, we use the JHK_s photometry measured by Bik et al. (2012) with LUCI on the Large Binocular Telescope for the sources where their photometry is more precise than 2MASS.

In addition, we consider whether any of the O- and B-type stars in W3 show infrared excess at longer wavelengths. Koenig et al. (2012) used 3.4, 4.6, 12, and 22 μm photometry from the *Wide-field Infrared Survey Explorer* (*WISE*), along with 2MASS JHK_s data, to identify and classify YSOs. About 2/3 of the 2MASS counterparts to the stars in our sample are found in the Koenig et al. (2012) catalog. Most of those have *WISE* colors consistent with stellar photospheres, but eight were classified by Koenig et al. (2012) as Class I (still enclosed in an infalling envelope) or Class II (optically thick disk) YSOs (see additional discussion in Section 3.4.)

Koenig et al. (2012) used a $3''$ radius to match *WISE* and 2MASS sources. The increasingly-large beam size at longer wavelengths means that source confusion becomes a concern, particularly in crowded fields like W3 Main. Two of our sources in W3 Main have apparent YSO-like infrared excess in Koenig et al. (2012): #25 (IRS N2) and #31 (IRS N4). For both sources, the offset between the 2MASS and *WISE* source positions is $> 2.5''$ and the association is likely spurious. Of the remaining six O- and B-type stars across W3 with YSO-like excesses, two (#29 and #60) have positional offsets of $> 1''$ and so their association with *WISE* sources should be treated with caution.

While *WISE* has neither the sensitivity nor the resolution of the *Spitzer Space Telescope*, *WISE* observations cover all of W3, unlike *Spitzer* surveys, which have mostly been limited to the HDL. Koenig et al. (2012) estimate that their sample of Class I and II YSOs in W3 is 90% complete down to $\sim$2–3 M$_\odot$, more than adequate for our study of the high-mass population.

3.4. *Comments on Spectral Features*

Binaries— The spectra of stars #21 and #61 show the two-component lines characteristic of double-lined spectroscopic binaries (SB2s). These systems have been the target of follow-up observations to characterize their orbital and physical parameters. Statistically, most of our sources are probably binaries (see discussion in Section 6), but our survey was not designed to identify or characterize source multiplicity.

Be Stars— Fourteen B stars, including one source from Navarete et al. (2011), exhibit definite Hα emission, with equivalent widths of 4–55 Å. (Source #65, shown in the right panel of Figure 4, has a typical level of Hα emission for this group.) Many of the Be stars display diverse spectral features at redder wavelengths: five (including the source from Navarete et al. 2011, not listed in Table 2) have double- or single-peaked Paschen line emission, three show narrow Paschen line absorption suggestive of a shell, and one has unusually strong metal absorption lines. Four Be stars are coincident with *WISE* Class I or II sources.

Infrared Excesses— As described in Section 3.3, six B stars, including four Be stars, are associated with *WISE* Class I or Class II sources from Koenig et al. (2012). The combination of YSO-like infrared excesses and Hα emission in these four Be stars suggests that they are Herbig Be stars, intermediate-to high-mass PMS stars in which the Hα emission is produced by accretion of material from a disk onto the star. However, we cannot rule out the possibility that these are classical Be stars, rapid rotators with Hα-emitting circumstellar disks and near-infrared excesses from free-free emission. The two non-Hα-emitting B stars with *WISE* infrared excesses are of similarly uncertain evolutionary state, as a lack of Hα emission does not rule out the presence of a disk.

3.5. *Spatial Distribution*

Figure 9 compares the distribution of dense gas in the HDL, as traced by ^{12}CO $J = 2$–1 emission

([Bieging & Peters 2011](#)), to the positions of the O- and B-type stars in W3. While the O-type stars are generally confined to the HDL, the early B-type (B0–3) and mid-to-late B-type (B4–9) stars are increasingly present toward the lower-density interior of the GMC and inside the W4 H II region. High-mass stars with *WISE* excess are also concentrated in the HDL, but several stars with Hα emission (also often considered a marker of youth) are found in the interior of the GMC. (A preliminary analysis of the spectra of the lower-mass stars in W3 has revealed additional Hα-emitting sources outside the HDL.) It is apparent from the observed mass segregation that, while star formation in W3 is occurring with the greatest vigor in the HDL, lower-level star formation has been (and may still be) taking place outside the prominent clusters.

4. THE EXTINCTION LAW TOWARD W3

Combining our 90Prime photometry with 2MASS data and B photometry from [Oey et al. (2005)](#) allows us to constrain the wavelength dependence of extinction for the line-of-sight toward W3. For each star, we compute as many as possible of the color excesses $E(B-V)$, $E(V-I)$, $E(V-J)$, and $E(V-K_s)$. The intrinsic colors for each spectral type are taken from [FitzGerald (1970)](#) and [Kenyon & Hartmann (1995)](#), with the Johnson J and K bands converted to 2MASS J and K_s using the transformations of [Sierchio et al. (2014)](#). The instrinsic colors of O-type stars from the more recent [Martins & Plez (2006)](#) study are slightly redder than those given by other references and do not align with the color scale for B-type stars. If we shift our entire intrinsic color scale to align with that of [Martins & Plez (2006)](#), the color excess ratios remain the same but the resulting extinctions decrease by an average of 0.13 mag.

To constrain the extinction at various wavelengths, we consider the parameter $R_{V\lambda}$, defined here as

$$R_{V\lambda} = \frac{A_V}{E(V-\lambda)} = \frac{1}{1 - A_\lambda/A_V}. \quad (1)$$

(We adopt the conventional notation R_V for the value of $A_V/E(B-V)$.) It can be shown that

$$R_{V\lambda} = \frac{E(V-K_s)/E(V-\lambda)}{1-(A_{Ks}/A_V)} \geq \frac{E(V-K_s)}{E(V-\lambda)}. \quad (2)$$

In Figure 10, we plot $E(V-K_s)$ against the other color excesses calculated for each star where available. We compute the slope of the relationship with a least-squares fit, fixing the intercept at zero under the assumption that zero extinction in any one filter means zero extinction in all observed filters. Only for the fit of $E(V-K_s)$ against $E(B-V)$ does this assumption have any effect on the calculated slope. From the color excess ratios, we find that $R_V \geq 3.17$, $R_{VI} \geq 2.27$, and $R_{VJ} \geq 1.26$. We note that R_V is at least 3.1, the average for the diffuse interstellar medium (ISM) in the Milky Way (e.g., [Rieke & Lebofsky 1985](#)), and greater than the $R_V \sim 2.9$ found for neighboring W4 by [Hanson & Clayton (1993)](#). The latter, however, is likely an artificially low estimate, as they assumed a spectrophotometric distance of 2.4 kpc to W3 in their analysis.

Lacking independent measures of the absolute magnitudes for any of our sources, we are unable to put upper limits on $R_{V\lambda}$ from our data alone. Instead, we turn to the range of A_{Ks}/A_V measurements in the literature in order to normalize our extinction law. Iterating on the R_V-dependent [Cardelli et al. (1989)](#) extinction law, we arrive at $R_V = 3.6$ for $A_{Ks}/A_V = 0.12$. Similarly, the equations of [Fitzpatrick & Massa (2009)](#) produce $R_V = 3.61$. Adopting $A_{Ks}/A_V = 0.12$, we find for W3 that $R_{VI} = 2.58$ and $R_{VJ} = 1.43$. The resulting extinction ratios are $A_V : A_I : A_J : A_{Ks} = 1 : 0.61 : 0.30 : 0.12$. These ratios are consistent with the [Cardelli et al. (1989)](#) extinction law for $R_V = 3.6$, with the higher-than-average R_V likely due to the contribution of larger grains in the W3 GMC. Using these values, the visual extinction toward the O- and B-type stars in W3 ranges from $A_V = 2.4$ mag to 12.2 mag, with an average of 5.7 mag.

In their study of massive stars in W3 Main, [Bik et al. (2012)](#) found that the [Nishiyama et al. (2008, 2009)](#) extinction law was the best fit for their JHK_s data. This extinction law, derived for sightlines toward the Galactic Center, has an unusually low A_{Ks}/A_V ratio of 0.062 ([Nishiyama et al. 2008](#)). If we adopt that value toward W3, we find that $R_V = 3.38$, $R_{VI} = 2.42$, $R_{VJ} = 1.34$, and the extinction ratios are $A_V : A_I : A_J : A_{Ks} = 1 : 0.59 : 0.25 : 0.06$. The resulting 4 : 1 ratio of $A_J : A_{Ks}$ is anomalously steep, even compared to that of [Nishiyama et al. (2008)](#), who found $A_J : A_{Ks} \sim 3:1$). For the rest of our analysis, we therefore adopt the more typical $A_{Ks}/A_V = 0.12$ described above. If we do use the lower A_{Ks}/A_V ratio, our resultant source luminosities decrease by a median of 0.15 dex, but our overall conclusions are unaffected.

5. HERTZSPRUNG-RUSSELL DIAGRAM

Using the extinction values from the previous section, we convert our observed stellar data to physical parameters and construct a Hertzsprung-Russell (H-R) diagram. Stellar temperatures are assigned based on spectral type: temperatures of O-type stars are from the "observational" scale of [Martins et al. (2005)](#) and those of B-type stars are from [Kenyon & Hartmann (1995)](#) and [Schmidt-Kaler (1982)](#). Observed V magnitudes are corrected for extinction and a distance of 2.0 kpc before bolometric corrections (BCs) applicable for each spectral type are applied. We use BCs from [Martins et al. (2005)](#) for all O-type stars, from [Kenyon & Hartmann (1995)](#) for B4-A1V stars, and from [Humphreys & McElroy (1984)](#) for BIII and B0-3V stars, to provide a smooth transition from O-type to B-type dwarfs.

The final H-R diagram is presented in Figure 11. Uncertainites on individual points for both temperature and luminosity are dominated by the uncertainties in spectral type. Luminosity values are also affected by the normalization of the extinction law, but for clarity we do not plot this systematic uncertainty. The majority of the stars are consistent with lying on the main sequence and there is no obvious main-sequence turnoff. Overall, there is no evidence for a population older than $\sim$10 Myr. Interstingly, the sources with Hα emission and/or *WISE* IR excess do not occupy any special location in the H-R diagram.

Three of the five hottest optically-detected stars in W3 belong to known star-forming clusters. BD+61°411 is an
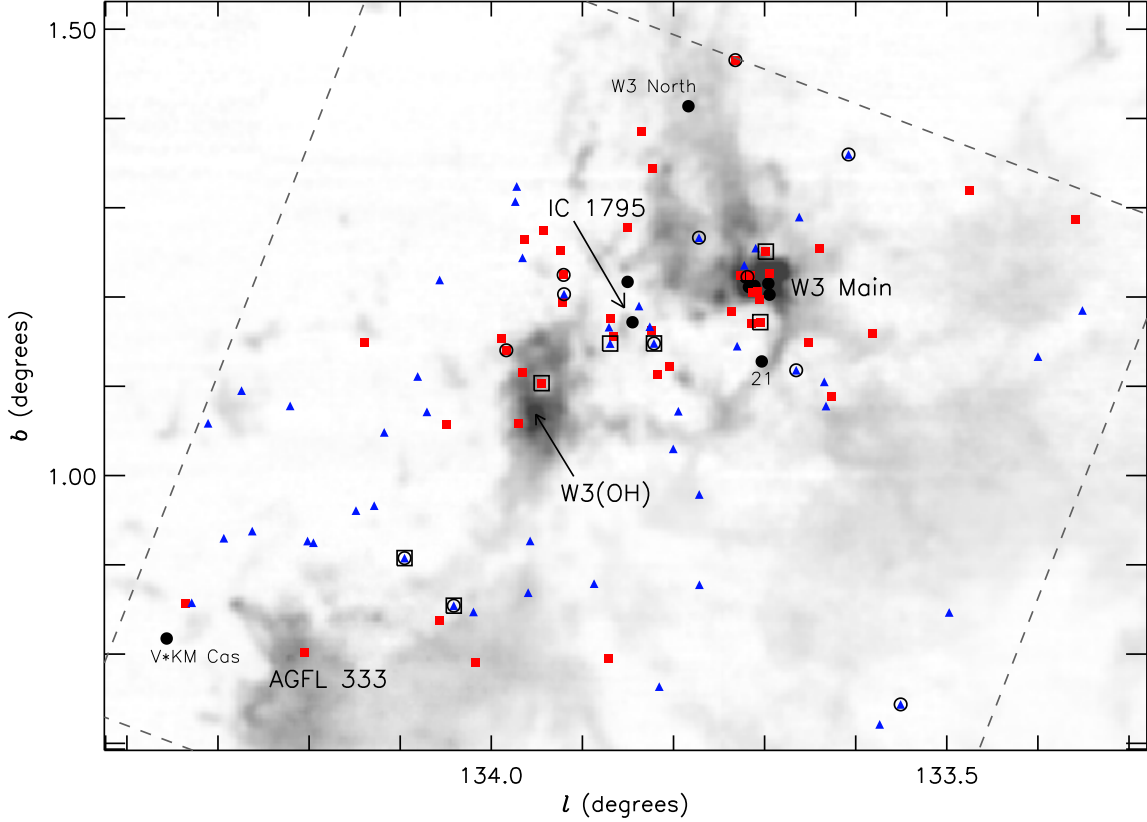
Figure 9. Spatial distribution of the O-type (black filled circles), early B-type (red filled squares), and mid-to-late B-type (blue filled triangles) stars in W3. The background is ^{12}CO $J = 2–1$ emission in the velocity range -60 to -25 km s^{-1} (Bieging & Peters 2011), which highlights the dense gas of the high-density layer (HDL) between the W3 GMC and the W4 H II region. Prominent features and specific stars of interest are labelled. Stars with Hα emission are marked with open circles, and stars with *WISE* IR excess are marked with open squares. The field of view of our 90Prime imaging is shown by the dashed lines.
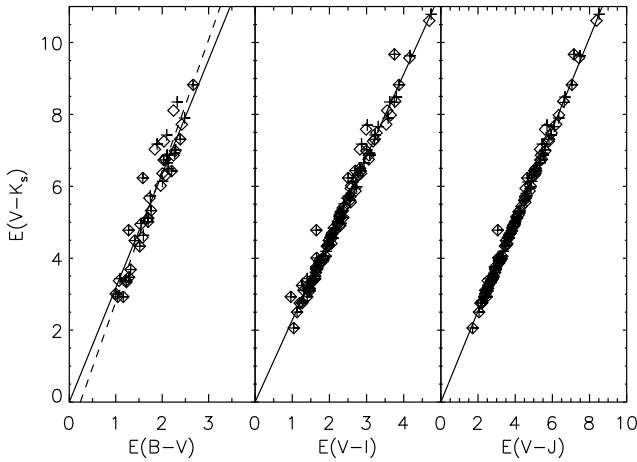

Figure 10. $E(V - K_s)$ versus other color excesses for O- and B-type stars in W3, used to constrain the extinction law in their direction. Pluses and open diamonds are values assuming a given star to be of the earliest and latest spectral type in its range, respectively (the two symbols lie atop each other for stars whose spectral type could be determined to within one subtype). Solid lines are least-squares fits to the points with the intercept fixed at zero, and the dashed line in the left plot is the fit for $E(B - V)$ versus $E(V - K_s)$ repeated without constraints on the intercept.

O6.5V((f)) star (Mathys 1989) that dominates the ionization budget of IC 1795, and NFD 559 (Navarete et al.

2011) is the visually-brightest member of W3 Main. Based on the positions of BD+61°411 and OWK 3041 in their H-R diagram, Oey et al. (2005) found a 3–5 Myr age spread for IC 1795 assuming $R_V = 2.9$ and a spectrophotometric distance of 2.3 kpc. We find the same age spread despite using a different distance and extinction law. In addition, the ~ 3 Myr age we estimate for NR 559 is consistent with the 1–3 Myr age for W3 Main found by Bik et al. (2012). (The youngest members of W3 Main are poorly represented in our H-R diagram because they are heavily extincted and therefore undetected in V.)

The two hottest optically-detected stars in W3 are W3 North, the ionizing star of a small H II region, and our source #21. Feigelson & Townsley (2008) did not detect any low-mass stars around W3 North in the X-ray, leading them to suggest that it was a runaway star ejected from IC 1795 or IC 1805. The observed age of ~ 2 Myr is broadly consistent with either scenario. Our source #21 is one of the serendipitiously-detected spectroscopic binaries and is composed of two O-type stars. This system does not appear to be associated with any known cluster, although it lies near a dense filament of the HDL (see Figure 9). Further study of the surrounding lower-mass population is necessary before we draw any conclusions about the origins of source #21.

The brightest star in W3 with Hα emission is NFD 3, a heavily-extincted object to the southeast of IC 1795. Navarete et al. (2011) identified this star as an evolved
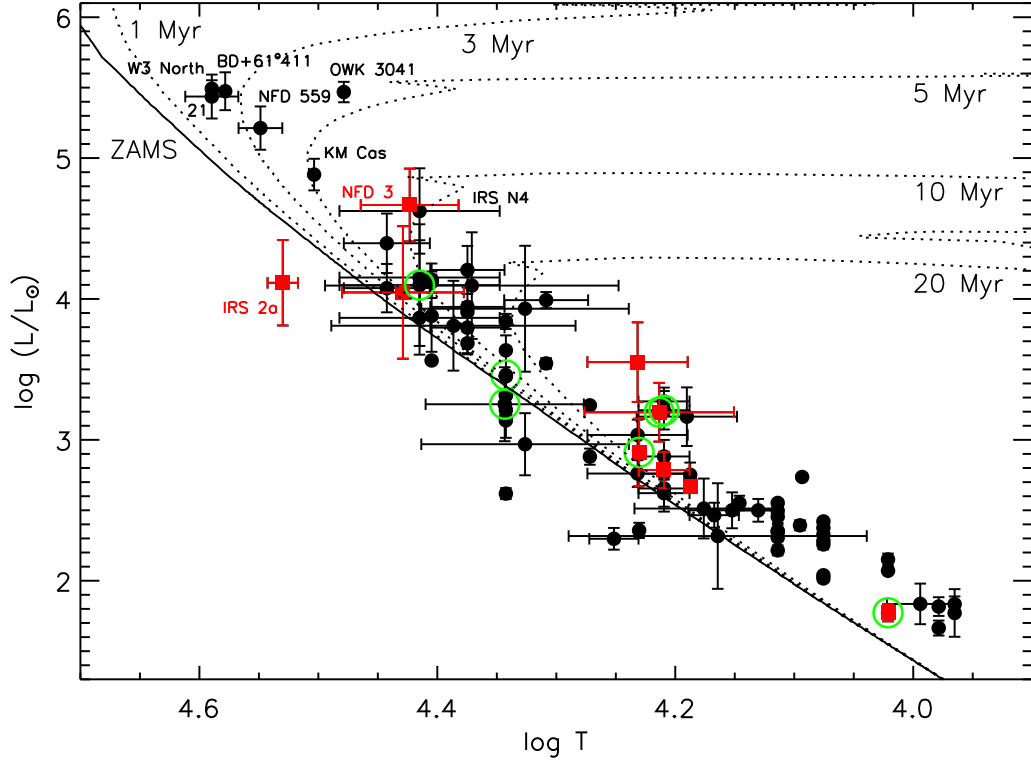
Figure 11. H-R diagram of the optically-detected high-mass stars in W3 for $R_V = 3.6$. Red filled squares and black filled circles are stars with and without Hα emission, respectively. Stars that show Class I or Class II *WISE* infrared excess according to Koenig et al. (2012) are circled in green. The solid line is the zero-age main sequence of Lejeune & Schaerer (2001) for a metallicity of $Z = 0.02$; the dotted lines are the 1, 3, 5, 10, and 20 Myr isochrones from the same model.

B0IIIe-B1IIIe based on its K-band spectrum. Although we observed this star with Hectospec, we were unable to confirm any spectral type from its optical features. However, this object's position in the H-R diagram is consistent with that of a star approaching the end of its main-sequence lifetime. As such, it is suggestive of a $\sim$ 10-Myr-old population in W3.

Another source of note is IRS N4 (our source #31), an early B-type star associated with the H II region W3 K in W3 Main. Bik et al. (2012) suggested that IRS N4 is a massive protostar still in the final stages of contraction to the ZAMS, a hypothesis consistent with its position on the outskirts of W3 Main but inconsistent with its visibility in V and its relatively mature H II region. It is possible that IRS N4, like NFD 3, is in fact a somewhat evolved star that formed before the rest of W3 Main.

A source that stands out in our H-R diagram is IRS 2a, an Hα-emitting O-type star lying noticeably below the ZAMS. IRS 2a is associated with the compact H II region W3 A in W3 Main (Ojha et al. 2004) and is therefore unlikely to be a background star. In addition, its known near-infrared excess (Bik et al. 2012) may have caused us to slightly overestimate its extinction: the A_V derived from $E(V - K_s)$ for IRS 2a is 1.3 mag higher than the A_V derived from $E(V - I)$. However, the relatively dense molecular material surrounding IRS 2a may have a higher R_V than the W3 average. Placing IRS 2a on or above the ZAMS requires that it have a minimum A_V of 11.3 mag, which translates to an R_V of 4.0 or greater. We note that the source in our sample with the highest

measured A_V, star #27 (NFD 386), is also located in the heart of W3 Main.

Finally, we note that KM Cas, the O-type star responsible for lighting up a bright-rimmed cloud near AFGL 333, is often considered a member of IC 1805. However, with our new determination of its extinction, the apparent age of KM Cas is 5 Myr, older than the 1–3 Myr age of the main IC 1805 cluster (Massey et al. 1995). This star is thus also consistent with the interpretation that star formation began in W3 before the current OB clusters appeared.

6. INITIAL MASS FUNCTION

We can gain additional insight into the high-mass stellar population of W3 by exploring the initial mass function (IMF). We assigned approximate masses to each star based on its spectral type: O-type stellar masses are from the "observational" scale of Martins et al. (2005); masses of unevolved B-type stars are derived by interpolating the $Z = 0.02$ ZAMS from Lejeune & Schaerer (2001) to the temperature for each type; and masses of evolved B-type stars are taken from the mass-spectral type relations of Drilling & Landolt (2000). None of the stars in W3 are massive enough to have experienced significant mass loss over their lifetimes (see, e.g., Smith 2014), so the current masses are representative of the inital masses. The resulting cumulative mass function is shown in Figure 12.

For stellar masses greater than approximately solar, the IMF is typically expressed as a power law of the form $dN/d(\log M) \propto M^{-\Gamma}$, where $\Gamma = 1.35$ is a Salpeter
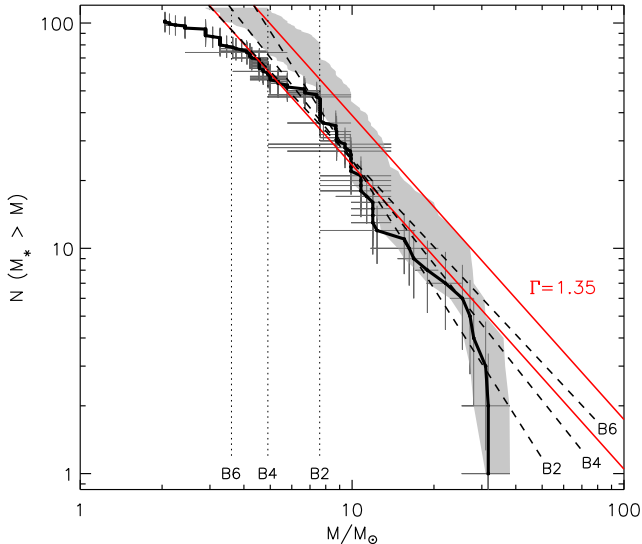
Figure 12. Cumulative initial mass function (IMF) for the 102 stars in our sample for which masses can be estimated. Least-squares fits to all stars more massive than B2, B4, and B6 dwarfs are shown as dashed lines, with the mass cutoffs marked with dotted lines. The grey shaded area illustrates the range of IMFs derived from Monte Carlo modelling of the unresolved binary population, assuming a flat mass distribution and a binary fraction of 50–90%. Salpeter (1955) IMFs normalized to the observed and binary-corrected IMFs at $5 M_\odot$ are overplotted for comparison (solid red lines).

(1955) IMF. We fit our cumulative histogram in logarithmic space with a straight line of the form $\log N(M_* > M) = a - \Gamma \log M$ using least-squares regression and treating the errors on $\log N$ as Poissonian (i.e., $\sigma_N = \sqrt{N}$). The use of a cumulative histogram instead of a standard one removes the slope dependence on bin size; however, the fit is still strongly dependent on the mass completeness limit. If we assume the sample is complete down to stars of type B6V, we find $\Gamma = 1.29$. For fits assuming that the sample becomes incomplete for types later than B4V and B2V, we find $\Gamma = 1.52$ and 1.90, respectively, as the fit increasingly emphasizes the steep upper end of the observed IMF.

The observational IMF is almost certainly undercounting the number of high-mass stars found in unresolved multiple systems. Half or more – perhaps even close to 100% – of massive star systems are multiples (Kiminki & Kobulnicky 2012; Sana et al. 2012). Furthermore, the mass ratio distribution of massive systems is roughly uniform, so massive stars are more likely to have massive companions than if their companions were drawn from a standard IMF (Kiminki & Kobulnicky 2012; Sana et al. 2012; Kobulnicky et al. 2014). Indeed, for two stars (see Section 3.4), we see evidence for similar-mass companions in the stellar spectra. Lack of evidence for binarity in the other observed systems is not evidence for a lack of companions, as we did not search for radial velocity variations and it was only by chance that the two SB2 systems were observed near quadrature.

We explore the effect of unresolved binaries on the IMF via a Monte Carlo simulation. Each star in our sample is randomly assigned a binarity status, assuming binary fractions between 50% and 90%. If a binary, we assign a

companion mass by drawing from a uniform mass ratio distribution between 0.005 and 1.0. The range of possible IMFs produced from 2000 repetitions of this simulation is shown in Figure 12. With binaries added, the IMF steepens slightly, but it remains consistent with Salpeter for $3 \lesssim M/M_\odot \lesssim 30$.

The drop-off of the observed IMF above 30 $M_\odot$ is likely the result of small-number statistics. The multi-cluster nature of W3 may also be responsible, since the relationship between cluster mass and the mass of its most massive star causes the observed high-mass IMF to steepen in composite populations (Weidner & Kroupa 2005). However, IC 1795 is old enough that a star of mass > 40 $M_\odot$, whose presence would fill out the top end of the W3 IMF, could have already gone supernova.

Assuming that the high-mass IMF in W3 is well-described by a Salpeter slope, we can extrapolate to estimate the size of the intermediate-mass stellar population. Normalizing a Salpeter IMF to account for unresolved binaries and the seven B-type stars without firm spectral types, we calculate that there are ∼900–1000 stars with M > 1 $M_\odot$ across W3. In comparison, Roccatagliata et al. (2011) identified 289 members and 340 candidate members of IC 1795 based on X-ray and IR data. Excluding the 100 or so of their sources with M < 1$M_\odot$, these numbers imply that 30–50% of the stars across our square-degree field of W3 are concentrated in a single cluster of radius 6′ in the HDL.

7. DISCUSSION AND CONCLUSIONS

With a wide-field imaging survey and multi-fiber spectroscopy, we have characterized 109 O- and B-type stars in the W3 star-forming region, including 83 previously unclassified sources (four of which are A-type stars). We have shown that the slope of the high-mass IMF in W3 is consistent with Salpeter ($\Gamma = 1.35$), and that the extinction toward W3 approximately follows the Cardelli et al. (1989) extinction law with $R_V \sim 3.6$.

Our detection of a population of B-type stars outside the HDL adds to the growing collection of evidence indicating that star formation has taken place throughout the W3 GMC. Our results corroborate the existence of the ∼ 8-Myr-old population detected in the K-band luminosity function by Román-Zúñiga et al. (2011), and we have identified a more distributed and possibly older population than that seen by Rivera-Ingraham et al. (2011) and Townsley et al. (2014). Diffuse stellar populations of this nature are common among star-forming regions of all sizes, ranging from Taurus (Slesnick et al. 2006) to Orion (e.g., Briceño et al. 2005) to the Carina Nebula Cluster (Feigelson et al. 2011), where more than half of the X-ray-identified young stars are found spread across a 50-pc region outside groups and clusters.

The H-R diagram of the O- and B-type stellar population in W3 also supports the interpretation that low-level star formation began throughout the W3 cloud 8–10 Myr ago. The timing of this initial star formation may have coincided with the first star formation episode in neighboring W4, which appears to have occurred 6–10 Myr ago (Dennison et al. 1997; Oey et al. 2005). However, it is clear from the spatial distribution of both the observed massive stars and the extrapolated intermediate-mass population that the star formation in W3 has been highly concentrated in the HDL over the past 3–5 Myr. Al-

though the association of increased star formation rates with dense gas surrounding an expanding superbubble is not direct evidence that the latter triggered the former (Dale et al. 2015), it is very suggestive of a causal relationship between feedback and accelerated star formation.

It remains possible that the observed distributed population in W3 is the remnant of an older cluster that has since dispersed. At the distance of W3 (2.0 kpc), a star with a transverse motion of 2 km s^{-1} will cover $\sim 17'$ in 10 Myr, allowing an unbound cluster to disperse over 2 deg^2. The presence of the W3 GMC is an argument against this hypothesis, however, as the natal cloud of an older cluster should have largely dispersed after 10 Myr (see, e.g., Leisawitz et al. 1989). *Gaia* will be able to test this possibility directly, as it is expected to measure the proper motions of $V = 18$ mag stars to a precision of 50 μas yr^{-1} (Perryman et al. 2001; Lindegren et al. 2008), which translates to 0.5 km s^{-1} at the distance of W3.

The next step to understanding the origin and history of the distributed stellar population in W3 is a study of the intermediate- and low-mass stars across the region. At 8–10 Myr after the commencement of star formation, stars less massive than ~ 2 M$_\odot$ will still be contracting toward the main sequence (Siess et al. 2000), potentially allowing a more precise age determination. Both early- and late-type B stars are expected to form surrounded by close groups of lower-mass stars (Testi et al. 1997); if such groups prove to be lacking, the argument for a dispersed cluster remnant is strengthened. Further analysis of our 90Prime and Hectospec observations will allow us to dig deeper into this complex star-forming region.

REFERENCES

Bertoldi, F. 1989, ApJ, 346,735

Bieging, J. H., & Peter, W. L. 2011, ApJS, 196, 18

Bik, A., Henning, Th., Stolte, A., et al. 2012, ApJ, 744, 87

Briceño, C., Calvet, N., Hernández, J., et al. 2005, AJ, 129, 907

Cardelli, J. A., Clayton, G. C., & Mathis, J. S. 1989, ApJ, 345, 245

Carpenter, J. M., Heyer, M. H., & Snell, R. L. 2000, ApJS, 130, 381

Dale, J. E., Haworth, T. J., & Bressert, E. 2015, MNRAS, 450, 1199

Dennison, B., Topsana, G. A., & Simonetti, J. H. 1997, ApJ, 474, L31

Drilling, J. S., & Landolt, A. U. 2000, in Allen's Astrophysical Quantities, ed. A. N. Cox (New York, NY: Springer-Verlag), 381

Elmegreen, B. G., & Lada, C. J. 1977, ApJ, 214, 725

Elmegreen, B. 1998, in ASP Conf. Ser. 148, Origins, ed. C. E. Woodward, J. Shull, & H. Thronson (San Francisco, CA: ASP), 150

Fabricant, D., Fata, R., Roll, J., et al. 2005, PASP, 117, 1411

Feigelson, E. D., Getman, K. V., Townsley, L. K., et al. 2011, ApJS, 194, 9

Feigelson, E. D., & Townsley, L. K. 2008, ApJ, 673, 354

FitzGerald, M. P. 1970, A&A, 4, 234

Fitzpatrick, E. L., & Massa, D. 2009, ApJ, 699, 1209

Gray, R. O., & Corbally, C. J. 2009, Stellar Spectral Classification (Princton, NJ: Princeton University Press)

Hachisuka, K., Brunthaler, A., Menten, K. M., et al. 2006, ApJ, 645, 337

Hanson, M. M., & Clayton, G. C. 1993, AJ, 106, 1947

Hirsch, L., Adams, J. D., Herter, T. L., et al. 2012, ApJ, 757, 113

Humphreys, R. M., & McElroy, D. B. 1984, ApJ, 284, 565

Kenyon, S. J., & Hartmann, L. 1995, ApJS, 101, 117

Kiminki, D. C., & Kobulnicky, H. A. 2012, ApJ, 751, 4

Kobulnicky, H. A., Kiminki, D. C., Lundquist, M. J., et al. 2014, ApJS, 213, 34

Koenig, X. P., Leisawitz, D. T., Benford, D. J., et al. 2012, ApJ, 744, 130

Lada, C. J., Elmegreen, B. G., Cong, H.-I., & Thaddeus, P. 1978, ApJ, 226, L39

Leisawitz, D., Bash, F. N., & Thaddeus, P. 1989, ApJS, 70, 731

Lejeune, T., & Schaerer, D. 2001, A&A, 366, 538

Lindegren, L., Babusiaux, C., Bailer-Jones, C., et al. 2008, in IAU Symp. 248, A Giant Step: from Milli- to Micro-arcsecond Astrometry, ed. W. J. Jin, I. Platais, & M. A. C. Perryman (Cambridge: Cambridge Univ. Press), 217

Markwardt, C. B. 2008, in ASP Conf. Ser. 411, Astronomical Data Analysis Software and Systems XVIII, ed. D. Bohlender, P. Dowler & D. Durand (San Francisco, CA: ASP), 25

Martins, F., & Plez, B. 2006, A&A, 457, 637

Martins, F., Schaerer, D., & Hillier, D. J. 2005, A&A, 436, 1049

Massey, P., Johnson, K. E., & DeGioia-Eastwood, K. 1995, ApJ, 454, 151

Mathys, G. 1989, A&AS, 81, 237

Megeath, S. T., Townsley, L. K., Oey, M. S., & Tieftrunk, A. R. 2008, in Handbook of Star Forming Regions, Vol. 1: The Northern Sky, ed. B. Reipurth (San Francisco, CA: ASP), 264

Mink, D. J., Wyatt, W. F., Caldwell, N., et al. 2007, in ASP Conf. Ser. 376, Astronomical Data Analysis Software and Systems XVI, ed. R. A. Shaw, F. Hill, & D. J. Bell (San Francisco, CA: ASP), 249

Navarete, F., Figueredo, E., Damineli, A., et al. 2011, AJ, 142, 67

Nishiyama, S., Nagata, T., Tamura, M., et al. 2008, ApJ, 680, 1174

Nishiyama, S., Tamura, M., Hatano, H., et al. 2009, ApJ, 696, 1407

Oey, M. S., Watson, A. M., Kern, K., & Walth, G. L. 2005, AJ, 129, 393

Ojha, D. K., Tamura, M., Nakajima, Y., et al. 2004, ApJ, 607, 797

Perryman, M. A. C., de Boer, K. S., Gilmore, G., et al. 2001, A&A, 369, 339

Polychroni, D., Moore, T. J. T., & Allsopp, J. 2012, MNRAS, 422, 2992

Rieke, G. H., & Lebofsky, M. J. 1985, ApJ, 288, 618

Rivera-Ingraham, A., Martin, P. G., Polychroni, D., & Moore, T. J. T. 2011, ApJ, 743, 39

Robin, A. C., Reylé, C., Derrière, S., & Picaud, S. 2003, A&A, 409, 523

Roccatagliata, V., Bouwman, J., Henning, Th., et al. 2011, ApJ, 733, 113

Román-Zúñiga, C. G., Megías-Vásquez, Alves, J. F., & Lada, E.
    A. 2011, in Stellar Clusters and Associations: A RIA Workshop
    on Gaia, ed. E. J. Alfaro Navarro, A. T. Gallego Calvente, &
    M. R. Zapatero Osorio (Granada, Spain), 141
Ruch, G. T., Jones, T. J., Woodward, C. E., et al. 2007, ApJ,
    654, 338
Salpeter, E. E. 1955, ApJ, 121, 161
Sana, H., de Mink, S. E., de Koter, A., et al. 2012, Science, 337,
    444
Sandford II, M. T., Whitaker, R. W., & Klein, R. I. 1982, ApJ,
    260, 183
Schmidt-Kaler, Th. 1982, in Landolt-Börnstein, Group VI, Vol.
    2., ed. K. Schaifers & H. H. Voigt (Berlin: Springer-Verlag), 454
Sierchio, J. M., Rieke, G. H., Su, K. Y. L., & Gáspár, A. 2014,
    ApJ, 785, 33
Siess L., Dufour E., & Forestini M. 2000, A&A, 358, 593
Slesnick, C. L., Carpenter, J. M., Hillenbrand, L. A., & Mamajek,
    E. E. 2006, AJ, 132, 2665
Skrutskie, M. F., Cutri, R. M., Stiening, R., et al. 2006, AJ. 131.
    1163

Smith, N. 2014, ARA&A, 52, 487
Stetson, P. B. 2000, PASP, 112, 925
Testi, L., Palla, F., Prusti, T., Natta, A., & Maltagliati, S. 1997,
    A&A, 320, 159
Townsley, L. K., Broos, P. S., Garmire, G. P., et al. 2014, ApJS,
    213, 1
Walborn, N. R., & Fitzpatrick, E. L. 1990, PASP, 102, 379
Weidner, C., & Kroupa, P. 2005, MNRAS, 365, 1333
Westerhout, G. 1958, Bull. Astron. Inst. Netherlands, 14, 215
Whitworth, A. P., Bhattal, A. S., Chapman, S. J., Disney, M. J.,
    & Turner, J. A. 1994, MNRAS, 268, 291
Williams, G. G., Olszewski, E., Lesser, M. P., & Burge, J. H.
    2004, Proc. SPIE, 5492, 787
Xu, Y., Reid, M. J., Zheng, X. W., & Menten, K. M. 2006,
    Science, 311, 54

Table 2
Photometry and Spectral Types of Candidate O- and B-Type Stars in W3

ID	α (J2000)	δ (J2000)	2MASS ID	Alternate IDs[a]	V (mag)	R (mag)	I (mag)	A_V[b] (mag)	Spectral Type	Comment[c]
1	02:22:39.64	+62:11:53.0	J02223962+6211528	$\cdots$	14.72 ± 0.03	$\cdots$	13.36 ± 0.03	3.6 ± 0.1	B7 V	$\cdots$
2	02:22:50.14	+61:49:48.1	J02225013+6149476	$\cdots$	16.43 ± 0.03	15.47 ± 0.03	14.48 ± 0.03	5.3 ± 0.1	B4–B7 V	$\cdots$
3	02:22:54.02	+62:07:57.7	J02225403+6207574	$\cdots$	15.20 ± 0.03	$\cdots$	13.66 ± 0.03	4.3 ± 0.1	B4–B5 V	$\cdots$
4	02:22:57.44	+61:42:53.8	J02225743+6142534	$\cdots$	15.99 ± 0.03	15.08 ± 0.03	14.18 ± 0.03	5.0 ± 0.0	B5 V	e
5	02:23:01.71	+62:17:29.4	J02230168+6217292	$\cdots$	15.92 ± 0.03	$\cdots$	13.82 ± 0.03	6.0 ± 0.0	B2 V	$\cdots$
6	02:23:04.47	+61:41:09.5	J02230445+6141093	$\cdots$	16.05 ± 0.03	15.18 ± 0.03	14.27 ± 0.03	4.7 ± 0.1	B9 V	$\cdots$
7	02:23:17.74	+61:35:31.4	J02231772+6135312	$\cdots$	16.50 ± 0.03	15.48 ± 0.03	14.34 ± 0.03	5.7 ± 0.2	B4–B5 V	e
8	02:24:03.54	+62:16:53.4	J02240353+6216531	$\cdots$	14.17 ± 0.03	$\cdots$	12.70 ± 0.03	4.2 ± 0.0	B3 V	$\cdots$
9	02:24:19.60	+61:27:40.7	J02241957+6127403	$\cdots$	16.61 ± 0.03	15.67 ± 0.03	14.69 ± 0.03	4.7 ± 0.1	A1 V	$\cdots$
10	02:24:25.89	+62:05:36.9	J02242588+6205365	$\cdots$	15.62 ± 0.03	14.27 ± 0.03	13.14 ± 0.03	6.9 ± 0.1	B0–B1 V	$\cdots$
11	02:24:35.01	+62:00:41.9	J02243501+6200417	$\cdots$	15.97 ± 0.03	14.63 ± 0.03	13.36 ± 0.03	7.3 ± 0.1	B1.5 V	$\cdots$
12	02:24:35.84	+61:59:58.6	J02243575+6159581	$\cdots$	17.77 ± 0.04	16.38 ± 0.03	15.05 ± 0.03	$\cdots$	B:	$\cdots$
13	02:24:41.63	+62:01:27.5	J02244164+6201271	$\cdots$	17.98 ± 0.03	16.63 ± 0.03	15.29 ± 0.03	$\cdots$	B:	$\cdots$
14	02:24:50.85	+61:32:05.2	J02245083+6132050	$\cdots$	15.06 ± 0.03	14.33 ± 0.03	13.57 ± 0.03	4.0 ± 0.1	B6 V	$\cdots$
15	02:24:57.74	+62:03:33.8	J02245771+6203335	$\cdots$	16.80 ± 0.03	15.48 ± 0.03	14.23 ± 0.03	7.2 ± 0.0	B2 V	$\cdots$
16	02:24:58.73	+62:01:32.0	J02245871+6201317	$\cdots$	17.06 ± 0.03	15.65 ± 0.03	14.21 ± 0.03	8.2 ± 0.4	B3–B5 V	e+Pa
17	02:25:06.11	+61:45:47.7	J02250608+6145476	$\cdots$	15.21 ± 0.03	14.47 ± 0.03	13.69 ± 0.03	4.0 ± 0.1	B7.5 V	$\cdots$
18	02:25:06.54	+61:38:27.3	J02250651+6138270	$\cdots$	15.27 ± 0.03	14.57 ± 0.03	13.86 ± 0.03	3.9 ± 0.1	B5–B6 V	$\cdots$
19	02:25:11.32	+62:09:43.0	J02251131+6209428	$\cdots$	15.85 ± 0.03	$\cdots$	13.94 ± 0.03	5.5 ± 0.0	B2 V	$\cdots$
20	02:25:15.03	+62:16:19.2	J02251502+6216191	$\cdots$	16.01 ± 0.03	$\cdots$	13.74 ± 0.03	$\cdots$	B:	e
21	02:25:18.59	+62:01:17.2	J02251857+6201169	$\cdots$	16.27 ± 0.03	14.48 ± 0.03	12.67 ± 0.03	10.1 ± 0.2	O5–O7 V	+O7–O9 V
22	02:25:24.38	+61:51:27.9	J02252435+6151277	$\cdots$	17.69 ± 0.04	16.13 ± 0.03	14.71 ± 0.03	$\cdots$	B:	$\cdots$
23	02:25:28.29	+62:11:14.2	J02252827+6211140	$\cdots$	16.19 ± 0.03	$\cdots$	14.35 ± 0.03	5.0 ± 0.2	B8 V	$\cdots$
24	02:25:31.68	+62:03:25.2	J02253167+6203249	$\cdots$	14.66 ± 0.03	13.52 ± 0.03	12.53 ± 0.03	6.3 ± 0.1	B1 V	$\cdots$
25	02:25:32.60	+62:06:59.8	J02253258+6206596	IRS N2	18.65 ± 0.04	$\cdots$	14.70 ± 0.03	10.8 ± 0.3	B1–B2 V	$\cdots$
26	02:25:34.63	+62:01:40.3	J02253461+6201401	$\cdots$	16.47 ± 0.03	15.51 ± 0.03	14.60 ± 0.03	5.1 ± 0.0	B7 V	$\cdots$
27	02:25:37.49	+62:05:24.8	J02253750+6205244	NFD 386	20.26 ± 0.09	17.94 ± 0.05	15.78 ± 0.03	12.2 ± 0.1	B0–B2 V[d]	$\cdots$
28	02:25:38.48	+61:39:01.0	J02253847+6139007	$\cdots$	14.23 ± 0.03	13.34 ± 0.03	12.45 ± 0.03	5.1 ± 0.1	B2 V	$\cdots$
29	02:25:38.81	+62:08:17.0	J02253880+6208168	$\cdots$	16.16 ± 0.03	14.90 ± 0.03	13.86 ± 0.03	6.7 ± 0.5	B2 V	e+sh+II
30	02:25:43.34	+62:06:15.7	J02254334+6206154	IRS 2a	19.41 ± 0.05	17.68 ± 0.04	15.92 ± 0.03	10.2 ± 0.6	O8–O9 V[e]	e
31	02:25:44.86	+62:03:41.5	J02254485+6203413	IRS N4	15.91 ± 0.04	14.19 ± 0.03	12.59 ± 0.03	9.0 ± 0.2	B0–B2 V[e]	$\cdots$
32	02:25:44.89	+62:08:15.8	J02254488+6208155	$\cdots$	16.43 ± 0.03	15.49 ± 0.03	14.53 ± 0.03	5.3 ± 0.2	B4–B5 V	$\cdots$
33	02:25:47.21	+61:53:43.3	J02254720+6153430	$\cdots$	16.90 ± 0.03	15.80 ± 0.03	14.74 ± 0.03	6.0 ± 0.1	B3–B5 V	$\cdots$
34	02:25:52.21	+61:56:12.3	J02255220+6156120	$\cdots$	16.28 ± 0.03	15.38 ± 0.03	14.48 ± 0.03	$\cdots$	B:	$\cdots$
35	02:26:01.10	+61:43:23.9	J02260110+6143237	$\cdots$	17.77 ± 0.03	16.56 ± 0.03	15.32 ± 0.03	6.6 ± 0.1	B5–B7 V	$\cdots$
36	02:26:05.87	+61:58:46.7	J02260587+6158465	$\cdots$	14.96 ± 0.03	13.97 ± 0.03	12.95 ± 0.03	5.7 ± 0.2	B1.5 V	$\cdots$
37	02:26:07.29	+62:02:55.1	J02260729+6202550	$\cdots$	15.62 ± 0.03	14.91 ± 0.03	14.20 ± 0.03	3.6 ± 0.3	A1 V	$\cdots$
38	02:26:10.50	+61:58:02.0	J02261050+6158018	$\cdots$	16.71 ± 0.03	15.68 ± 0.03	14.60 ± 0.03	5.9 ± 0.1	B3 V	$\cdots$
39	02:26:16.90	+62:07:35.2	J02261690+6207350	$\cdots$	17.62 ± 0.03	16.00 ± 0.03	14.25 ± 0.03	$\cdots$	B:	e+pec
40	02:26:17.35	+61:29:42.3	J02261734+6129420	$\cdots$	17.95 ± 0.04	16.72 ± 0.03	15.44 ± 0.03	6.8 ± 0.2	B3–B9 V	$\cdots$
41	02:26:18.80	+61:59:53.1	J02261880+6159529	$\cdots$	15.17 ± 0.03	14.41 ± 0.03	13.67 ± 0.03	4.6 ± 0.5	B4 V	e+Pa+II
42	02:26:22.90	+62:00:37.3	J02262290+6200370	$\cdots$	15.41 ± 0.03	14.25 ± 0.03	13.12 ± 0.03	6.5 ± 0.1	B1–B2 V	$\cdots$
43	02:26:23.39	+61:28:45.3	J02262338+6128449	$\cdots$	14.49 ± 0.03	13.97 ± 0.03	13.42 ± 0.03	2.9 ± 0.0	B9 V	$\cdots$
44	02:26:24.42	+62:00:50.4	J02262442+6200501	$\cdots$	17.52 ± 0.04	16.03 ± 0.03	14.58 ± 0.03	7.8 ± 0.2	B4–B6 V	$\cdots$
45	02:26:33.49	+61:41:16.7	J02263349+6141164	$\cdots$	16.42 ± 0.03	15.40 ± 0.03	14.20 ± 0.03	6.2 ± 0.1	B3–B5 V	$\cdots$
46	02:26:34.32	+62:01:53.0	J02263433+6201527	$\cdots$	14.38 ± 0.03	13.78 ± 0.03	13.12 ± 0.03	3.8 ± 0.1	B4–B5 V	$\cdots$
47	02:26:34.39	+62:19:35.3	J02263439+6219350	$\cdots$	$\cdots$	$\cdots$	$\cdots$	$\cdots$	B0–B4 V	e+sh
48	02:26:41.31	+61:59:24.6	J02264129+6159242	OWK 1007	14.27 ± 0.03	13.63 ± 0.03	12.96 ± 0.03	3.9 ± 0.3	B2 V	$\cdots$
49	02:26:41.74	+61:58:50.6	J02264173+6158503	$\cdots$	17.68 ± 0.04	16.23 ± 0.03	14.75 ± 0.03	7.9 ± 0.1	B4–B5 V	I
50	02:26:43.00	+61:44:34.2	J02264301+6144339	$\cdots$	15.18 ± 0.03	14.47 ± 0.03	13.67 ± 0.03	4.2 ± 0.1	B5 V	$\cdots$
51	02:26:45.71	+61:59:50.7	J02264570+6159504	$\cdots$	16.76 ± 0.03	15.72 ± 0.03	14.66 ± 0.03	5.7 ± 0.1	B6–B7 V	$\cdots$
52	02:26:46.42	+61:35:39.1	J02264642+6135387	$\cdots$	17.44 ± 0.04	15.66 ± 0.03	13.95 ± 0.03	9.5 ± 0.2	B0–B4 V	$\cdots$
53	02:26:46.65	+62:00:26.2	J02264664+6200259	OWK 4012	13.92 ± 0.03	13.25 ± 0.03	12.57 ± 0.03	4.0 ± 0.2	B2 V	$\cdots$
54	02:26:55.49	+62:10:51.9	J02265547+6210516	$\cdots$	15.75 ± 0.03	14.45 ± 0.03	13.13 ± 0.03	7.3 ± 0.3	B1 V	$\cdots$
55	02:26:56.28	+62:06:31.5	J02265627+6206313	$\cdots$	16.27 ± 0.03	14.94 ± 0.03	13.59 ± 0.03	7.6 ± 0.2	B0–B3 V	$\cdots$

Table 2 — *Continued*

ID	α (J2000)	δ (J2000)	2MASS ID	Alternate IDs[a]	V (mag)	R (mag)	I (mag)	A_V[b] (mag)	Spectral Type	Comment[c]
56	02:26:57.50	+61:38:49.3	J02265752+6138489	$\cdots$	17.18 ± 0.03	16.33 ± 0.03	15.39 ± 0.03	4.9 ± 0.2	A0 V	$\cdots$
57	02:26:57.89	+61:38:46.6	J02265789+6138462	$\cdots$	15.30 ± 0.03	14.53 ± 0.03	13.71 ± 0.03	4.3 ± 0.0	B8 V	$\cdots$
58	02:27:09.17	+62:12:53.0	J02270916+6212528	OWK 7003	14.86 ± 0.03	13.70 ± 0.03	12.50 ± 0.03	7.0 ± 0.2	B0–B1 V	$\cdots$
59	02:27:09.36	+61:38:41.8	J02270936+6138415	$\cdots$	16.75 ± 0.03	15.97 ± 0.03	15.15 ± 0.03	4.4 ± 0.1	B9 V	e+I
60	02:27:09.40	+61:54:44.0	J02270938+6154437	$\cdots$	17.44 ± 0.03	16.16 ± 0.03	14.83 ± 0.03	7.3 ± 0.2	B1–B3 V	I
61	02:27:12.91	+61:51:39.2	J02271290+6151390	$\cdots$	14.52 ± 0.03	13.49 ± 0.03	12.45 ± 0.03	6.0 ± 0.1	B1–B2 V	+B3–B4 V
62	02:27:13.93	+61:37:25.5	J02271392+6137251	$\cdots$	15.63 ± 0.03	14.43 ± 0.03	13.15 ± 0.03	7.2 ± 0.2	B1 V	$\cdots$
63	02:27:15.13	+62:00:15.3	J02271510+6200151	$\cdots$	14.73 ± 0.03	13.66 ± 0.03	12.57 ± 0.03	6.1 ± 0.1	B2 V	$\cdots$
64	02:27:16.04	+62:00:50.8	J02271602+6200506	$\cdots$	16.38 ± 0.03	14.77 ± 0.03	13.15 ± 0.03	$\cdots$	B:	e+Pa
65	02:27:20.25	+62:02:02.6	J02272023+6202023	$\cdots$	16.10 ± 0.03	14.82 ± 0.03	13.49 ± 0.03	7.6 ± 0.6	B0–B1.5 V	e+sh
66	02:27:21.36	+61:54:57.3	J02272133+6154570	NFD 252	17.57 ± 0.04	15.83 ± 0.03	14.16 ± 0.03	9.2 ± 0.6	B1–B4 V	$\cdots$
67	02:27:39.55	+61:56:33.3	J02273953+6156330	$\cdots$	17.39 ± 0.04	15.86 ± 0.03	14.32 ± 0.03	8.6 ± 0.1	B0–B2 V	$\cdots$
68	02:27:40.20	+62:04:20.0	J02274017+6204197	$\cdots$	17.06 ± 0.03	15.94 ± 0.03	14.81 ± 0.03	6.4 ± 0.1	B1–B4 V	$\cdots$
69	02:27:44.58	+61:40:30.3	J02274456+6140299	$\cdots$	16.41 ± 0.03	15.17 ± 0.03	13.95 ± 0.03	6.8 ± 0.2	B3–B6 V	e+Pa+II
70	02:27:45.34	+62:02:08.0	J02274532+6202078	$\cdots$	14.44 ± 0.03	13.87 ± 0.03	13.30 ± 0.03	3.2 ± 0.1	B4–B5 V	$\cdots$
71	02:27:48.33	+62:03:19.8	J02274831+6203196	$\cdots$	14.31 ± 0.03	13.55 ± 0.03	12.80 ± 0.03	4.5 ± 0.0	B1 V	$\cdots$
72	02:27:50.29	+61:49:51.7	J02275028+6149514	$\cdots$	18.11 ± 0.04	16.94 ± 0.03	15.76 ± 0.03	6.4 ± 0.1	B2 V	$\cdots$
73	02:28:00.86	+62:05:28.9	J02280084+6205285	$\cdots$	17.23 ± 0.03	16.23 ± 0.03	15.25 ± 0.03	5.2 ± 0.1	B8 V	$\cdots$
74	02:28:01.73	+61:51:39.8	J02280172+6151395	$\cdots$	14.45 ± 0.03	13.97 ± 0.03	13.42 ± 0.03	2.4 ± 0.2	A0 V	$\cdots$
75	02:28:03.19	+61:50:11.9	J02280319+6150116	$\cdots$	16.35 ± 0.03	15.32 ± 0.03	14.31 ± 0.03	5.5 ± 0.1	B7 V	$\cdots$
76	02:28:03.28	+62:06:27.7	J02280324+6206276	$\cdots$	14.23 ± 0.03	13.37 ± 0.03	12.54 ± 0.03	4.6 ± 0.1	B4–B5 V	$\cdots$
77	02:28:11.11	+61:43:03.7	J02281111+6143034	$\cdots$	15.57 ± 0.03	14.76 ± 0.03	13.94 ± 0.03	4.5 ± 0.0	B8 V	$\cdots$
78	02:28:15.35	+61:52:11.5	J02281533+6152112	$\cdots$	17.26 ± 0.03	16.29 ± 0.03	15.30 ± 0.03	5.3 ± 0.0	B8 V	$\cdots$
79	02:28:16.93	+61:32:11.0	J02281694+6132102	$\cdots$	15.00 ± 0.03	13.79 ± 0.03	12.54 ± 0.03	6.9 ± 0.1	B2–B3 V	$\cdots$
80	02:28:19.51	+61:42:18.9	J02281951+6142185	$\cdots$	16.75 ± 0.03	15.83 ± 0.03	14.91 ± 0.03	4.8 ± 0.2	B9–A1 V	$\cdots$
81	02:28:21.11	+61:47:53.4	J02282111+6147531	$\cdots$	17.91 ± 0.04	16.81 ± 0.03	15.69 ± 0.03	5.9 ± 0.1	B4 V	$\cdots$
82	02:28:24.03	+61:58:45.5	J02282402+6158452	$\cdots$	15.48 ± 0.03	14.53 ± 0.03	13.51 ± 0.03	5.4 ± 0.0	B8 III	$\cdots$
83	02:28:34.86	+61:39:16.8	J02283486+6139165	$\cdots$	17.93 ± 0.03	16.93 ± 0.03	15.82 ± 0.03	5.7 ± 0.1	B3–B4 V	$\cdots$
84	02:28:38.24	+61:39:14.7	J02283823+6139144	$\cdots$	15.57 ± 0.03	14.84 ± 0.03	14.03 ± 0.03	4.2 ± 0.1	B8 V	$\cdots$
85	02:28:50.20	+61:53:01.2	J02285019+6153009	$\cdots$	16.09 ± 0.03	15.07 ± 0.03	14.02 ± 0.03	5.9 ± 0.0	B2 V	$\cdots$
86	02:29:08.84	+61:38:31.6	J02290883+6138314	$\cdots$	14.48 ± 0.03	13.94 ± 0.03	13.35 ± 0.03	3.7 ± 0.2	B5 V	$\cdots$
87	02:29:15.41	+61:47:16.3	J02291539+6147160	$\cdots$	14.97 ± 0.03	14.34 ± 0.03	$\cdots$	3.6 ± 0.1	B8 V	$\cdots$
88	02:29:22.00	+61:37:23.6	J02292199+6137234	$\cdots$	14.12 ± 0.03	13.58 ± 0.03	13.03 ± 0.03	3.1 ± 0.0	B7 V	$\cdots$
89	02:29:25.08	+61:32:34.9	J02292506+6132347	$\cdots$	15.14 ± 0.03	14.56 ± 0.03	13.95 ± 0.03	3.4 ± 0.1	B7 V	$\cdots$
90	02:29:43.79	+61:47:02.6	J02294376+6147023	$\cdots$	14.98 ± 0.03	14.31 ± 0.03	13.63 ± 0.03	3.6 ± 0.1	B7 V	$\cdots$
91	02:29:54.22	+61:44:11.2	J02295419+6144110	$\cdots$	14.68 ± 0.03	14.11 ± 0.03	13.52 ± 0.03	3.2 ± 0.1	B7 V	$\cdots$

[a] OWK = Oey et al. (2005); NFD = Navarete et al. (2011); IRS = named infrared source in W3 Main, see Ojha et al. (2004) and Bik et al. (2012).

[b] For $R_V = 3.6$ (see Section 4).

[c] e = Hα emission; Pa = Paschen emission; sh = shell features; pec = peculiar metal line absorption; I(II) = *WISE* Class I(II) YSO from Koenig et al. (2012).

[d] Spectral type from Navarete et al. (2011).

[e] Spectral type from Bik et al. (2012).